Chemical Science

ROYAL SOCIETY OF CHEMISTRY

EDGE ARTICLE

View Article Online
View Journal | View Issue

Cite this: *Chem. Sci.*, 2024, **15**, 1679

All publication charges for this article have been paid for by the Royal Society of Chemistry

Received 21st October 2023
Accepted 19th December 2023

DOI: 10.1039/d3sc05644a

rsc.li/chemical-science

Hydrous ruthenium oxide triggers template-free and spontaneous growth of metal nanostructures†

Faheem Muhammad,‡[a] Xiwen Chen,‡[a] Jiayi Tang,‡[a] Yuan Cheng,[a] Yuyang Li,[b] Chenxin Zhu,[a] Yihong Zhang,[a] Leiying Miao,[b] Yu Deng[a] and Hui Wei *[ac]

Intrinsically conductive ruthenium oxide is an excellent material for energy storage and conversion. Herein, we present hydrous RuO_2 (H–RuO_2) as a potent reducing agent to achieve spontaneous growth of multiple noble metals at room temperature. Self-assembled gold and platinum, comprising small-sized nanoparticles, are generated on the surface of H–RuO_2 without the need for additional templates. Structural analysis reveals that the disordered structure and the presence of oxygen vacancies trigger interfacial redox reactions between H–RuO_2 and oxidative metal salts. The resulting integrated nanostructures, consisting of a metal oxide and different metals (H–RuO_2@metal), are subsequently used to treat inflammatory bowel diseases. In addition to biomedical applications, our developed synthetic strategy, using reactive oxides to spontaneously generate multicomponent nanostructures, also holds great significance for other catalysis-based applications.

Introduction

The fabrication of multicomponent nanomaterials to attain unique chemical, optical, and electronic properties inaccessible in a single component has attracted tremendous research activity over the last two decades.[1–6] Such nanomaterials exist in numerous designs, including core–shell, yolk–shell, Janus, dots-on-nanorods, dots-in-nanotubes, nanobranched, and heterodimer.[7–13] Among various chemical compositions, metal oxide supported multicomponent nanomaterials have gained immense importance due to their enhanced and unanticipated catalytic activities originating from multiple phenomena, encompassing strong metal support interactions, modified electronic band structures, the availability of plasmonic hot electrons, and improved durability.[14–18]

Both physical and chemical methods are used to synthesize metal oxide-supported noble metals. Physical strategies include laser-induced heating,[19] ion beam co-sputtering,[20] ion implantation,[21] and carbothermal shock methods.[22] Chemical methods are however preferred because of the flexibility they offer in producing controllable products with improved catalytic performance. Chemical synthesis is typically carried out with the aid of external reducing agents such as gaseous hydrogen, oleylamine, sodium borohydride, hydrazine, ascorbic acid, *etc.* to reduce the oxidative noble metal salts. During synthesis, the metal oxide supports merely act as spectators.[23–25] Recently, there have been a few reports wherein metal oxide supports also actively participated in redox reactions, spontaneously converting noble metal salts into metal nanoparticles (NPs) without using any external reducing agents. For instance, Lee *et al.* used MnO_x as a reactive oxide to deposit ultrasmall Pt NPs.[26] Other metal oxides, such as CeO_2, TiO_2, FeO_x, and WO_3, have also shown similar redox properties.[27–31] However, in previously reported reactive oxide systems, harsh pretreatments were required to transform a non-reactive oxide into a reactive one by introducing defects (oxygen vacancies) in the crystal structure; moreover, the spontaneously growing metals were also invariably produced in the form of spherical isolated NPs and the growth of metal NPs on the surface of a reactive oxide was achieved at rather high temperatures. In this study, we present as-synthesized H–RuO_2 as a more stable and effective reducing agent to spontaneously generate noble metals at room temperature with self-assembled nanostructures due to the high conductivity (~1 S cm^{-1}) and the strong reducing power of H–RuO_2.

In addition to developing new synthetic protocols for multicomponent nanomaterials, a great deal of research activity has also been witnessed over the last decade in biocatalytic nanoscale materials (namely nanozymes). Nanozymes display superior characteristics compared to their natural counterparts and have been explored for a wide variety of applications.[32–36] A

[a]*College of Engineering and Applied Sciences, Nanjing National Laboratory of Microstructures, Jiangsu Key Laboratory of Artificial Functional Materials, Nanjing University, Nanjing, Jiangsu 210023, China. E-mail: weihui@nju.edu.cn*

[b]*Department of Cariology and Endodontics, Nanjing Stomatological Hospital, Medical School of Nanjing University, Nanjing 210008, China*

[c]*State Key Laboratory of Analytical Chemistry for Life Science, School of Chemistry and Chemical Engineering, Chemistry and Biomedicine Innovation Center (ChemBIC), Nanjing University, Nanjing, Jiangsu 210023, China*

† Electronic supplementary information (ESI) available. See DOI: https://doi.org/10.1039/d3sc05644a

‡ These authors contributed equally to this work.

wide range of materials, including metals, metal oxides,[37] sulphides,[38] metal–organic frameworks,[39,40] single-atom,[41] and carbon-based materials, have been explored to mimic natural enzymes.[42] The well-proven catalytic properties and the chemical stabilities of both H–RuO_2 and spontaneously grown noble metal nanostructures motivated us to explore them as nanozymes.[43–45] The obtained integrated structures of these diverse materials demonstrated significantly high superoxide dismutase (SOD)- and catalase (CAT)-like activities. The ROS scavenging features of the H–RuO_2@metal nanostructures were successfully translated into *in vivo* models for the treatment of inflammatory bowel diseases (IBDs).

Results and discussion

We first developed a facile synthetic protocol to produce large-scale ultrasmall H–RuO_2 NPs ($RuO_2 \cdot xH_2O$ or RuO_xH_y) (Fig. S1†). The multidentate character of the surface-bound citrate moieties ensured the anchoring of noble metal precursors, which were spontaneously reduced on the surface of H–RuO_2 in the subsequent steps. The low synthetic temperature (80 °C) used to synthesize H–RuO_2 also raised the probability of oxygen vacancies because of the incomplete conversion of trivalent ruthenium hydroxide into RuO_2.[46–48] The understanding of oxygen vacancy and the ensuing changes in the

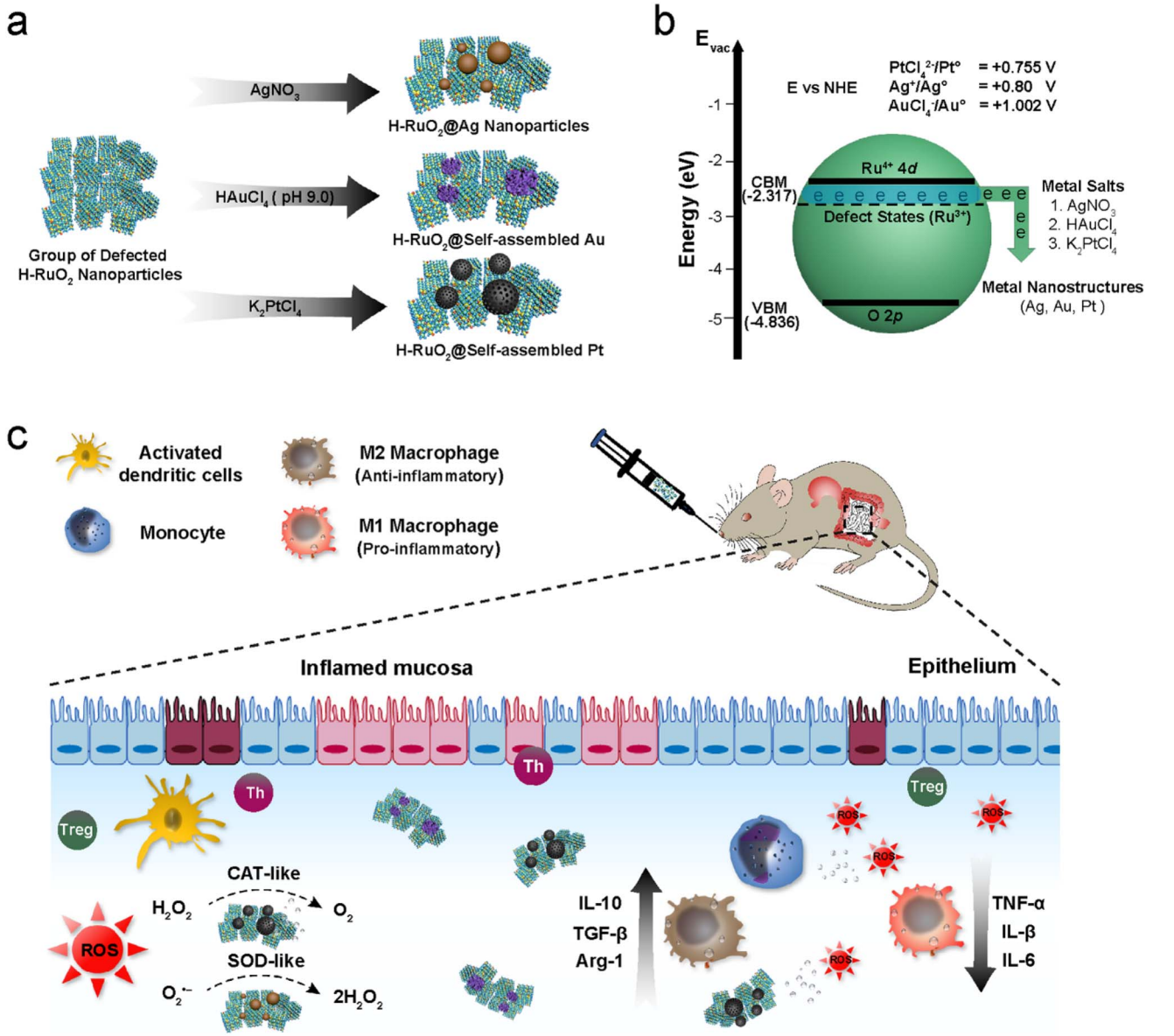

Fig. 1 Schematic illustrations depicting the synthetic conditions, mechanism, and subsequent utilization of H–RuO_2@metal nanostructures as nanozymes in treating inflammatory bowel diseases. (a) Schematic diagram showing the synthetic protocol used for the spontaneous growth of noble metal nanostructures on the surface of H–RuO_2. (b) Scheme elucidating the oxygen vacancy-mediated appearance of energy states in defect-containing H–RuO_2 NPs and the ensuing interfacial redox reactions of oxidative metal precursors in the growth of metal nanostructures. (c) Schematic diagram showing the multiple enzyme-like activities of H–RuO_2@metal in treating IBD.

electronic structure of the materials are of paramount importance to deciphering the spontaneous growth mechanism of noble metals. In principle, when an O atom is removed from the crystal lattice of a metal oxide, it leaves excess electrons (two electrons per oxygen vacancy around the nearest neighbours) leading to the introduction of new electronic states below the conduction band minimum (CBM).[49,50] The appearance of electronic states in the forbidden band structure and the dynamical nature of the structural defect impart a metallic character to oxygen-deficient metal oxides.[51] In addition to the oxygen vacancy-induced metallic character, the H–RuO_2 itself also has an intrinsic metallic character due to free d-electrons. Hence, the high conductivity and trapped electrons in H–RuO_2 can best act as an efficient reducing agent to spontaneously generate different metal nanostructures under mild conditions. To validate the redox active behaviour and the presence of oxygen vacancies in H–RuO_2, we performed a parallel study wherein commercial RuO_2 was tested along with H–RuO_2 NPs.

As illustrated in Fig. 1b, the reduction potential of the defect-induced electronic states of H–RuO_2 NPs is thermodynamically more negative than the redox potentials of the selected metal precursors (*i.e.*, +1.002, +0.755, and +0.800 V *vs.* NHE for $HAuCl_4$, K_2PtCl_4, and $AgNO_3$, respectively). Hence, upon adding the respective oxidative metal precursors into the H–RuO_2 solution at room temperature, the heterogeneous interfacial redox reactions led to the spontaneous growth of noble metal nanostructures with different reaction kinetics (Fig. 1a). Gold salt was the first to be promptly reduced and nucleated on H–RuO_2 NPs because it has the highest positive reduction potential of the three metal precursors. To tune the growth rate, the pH of the solutions was changed, and as a result, variable nanostructures of Au were produced. In an acidic solution, large-sized Au NPs were produced, whereas self-assembled structures were generated in alkaline pH without using any templates. The formation of the self-assembled Au nanostructure, composed of small-sized NPs, is likely due to the lowering of the rate of a redox reaction. Under alkaline conditions, hydroxylated Au species such as $AuCl_3(OH)^-$, $AuCl_2(OH)_2^-$, and $AuCl(OH)_3^-$ are formed. Fig. S2† elucidates and tracks the formation of self-assembled gold. The spontaneous growth of Ag NPs was also observed within minutes; the colour of the reaction solution rapidly changed from forest green to black. The products of H–RuO_2@Ag were analyzed at different points in time; a progressive enlargement of Ag was observed when the duration of the reaction was increased to 24 h (Fig. S3†). Regarding the growth of platinum, the reduction/growth rate of Pt was the slowest among the three tested metals (0.755 V). The growth evolution of self-assembled Pt indicated that at first small-sized Pt NPs (nuclei) were produced, as shown in Fig. S4.† The self-assembly of those 3 nm-sized NPs became apparent after 3 h incubation of the metal salt with H–RuO_2 (Fig. S4b†). A well-defined platinum was consequently formed after 24 h reaction. To accelerate the growth of Pt, the product was also synthesized at a higher temperature (80 °C). Nitrogen adsorption analysis was performed to determine the porosity of the nanostructures; the BET surface areas can be seen in Fig. S5.† Our findings regarding the growth mechanism indicated that two factors regulate the final structures of the noble metals: (1) pH is the main contributor in the case of Au; the fast reduction rate under acidic conditions gives rise to the formation of isolated large-sized Au NPs, whereas the alkaline pH lowers the reduction kinetics, favoring the production of self-assembled structures, and (2) the oriented attachment of small-sized Au and Pt NPs along a common crystallographic direction in a bid to minimize the interfacial energy of small NPs led to the production of self-assembled structures. In all these redox reactions between metal precursors and H–RuO_2, the excess electrons localized in the Ru 3d orbital of low-coordinated ruthenium atoms (Ru^{3+}) near the site of the oxygen vacancy likely participated in the growth of metal nanostructures. For comparison, the metal salts were also exposed to commercial RuO_2 NPs under identical experimental conditions. No apparent change in the colour of the solutions was noticed, indicating the inactive nature of the commercial RuO_2 in reducing the metal precursors.

Using transmission electron microscopy (TEM) and high-angle annular dark-field scanning transmission electron microscopy (HAADF-STEM), the size, morphology, and crystalline nature of both commercial and H–RuO_2 NPs were examined. A disordered crystal structure was observed in the H–RuO_2 product (~2 nm); in contrast, agglomerated polycrystalline NPs (50–100 nm) could be seen in the HRTEM image of commercial RuO_2 (Fig. 2); EDX elemental mapping shows the composition of both materials, composed of Ru and O. To examine oxygen vacancies in H–RuO_2, aberration-corrected STEM images were acquired but could not collect the desired results due to the ultrasmall size of H–RuO_2 NPs (Fig. 2b). The electron energy loss spectroscopy (EELS) method was therefore used; the Ru-$M_{4,5}$ and O-K signals detected from the selected areas are shown in Fig. 2k. We specifically analysed the O-K-pre-edge area because of the overlap of Ru-$M_{4,5}$ and C-K ionization edges. The spectrum of commercial RuO_2 shows two prominent peaks (529.7 eV and 532.4 eV): the first pre-edge peak can be related to the transition from the O 1s core level to the O 2p component hybridized with the Ru 4d level, and the second peak is attributed to the unoccupied O 2p states hybridized with the Ru 5s and 5p states. An apparent decrease in the intensities of both peaks was observed in the case of H–RuO_2, especially the peak present at 529.7, implying the presence of a considerable number of vacancies. In addition, highlighted as dotted lines, the O-K onset energy (~528 eV) in H–RuO_2 was also found to be lower than that of commercial RuO_2 (~529 eV), which suggested the existence of a lower oxidation state of ruthenium (Ru^{3+}) in H–RuO_2. The band structure and the presence of the oxygen defect-induced donor states in commercial and H–RuO_2 NPs were probed by ultraviolet photoelectron spectroscopy (UPS). The relative positions of the valence band maximum (VBM) and the conduction band minimum (CBM) of both samples were acquired, as shown in Table S1;† the band gaps (E_g) of the samples were calculated from the absorption spectra using the Tauc plot method (Fig. S6†). In the UPS valence-band spectrum of H–RuO_2, oxygen vacancy-associated donor states near the Fermi level can be seen in Fig. 2l (highlighted as a green circle). The availability of such donor states near the conduction band

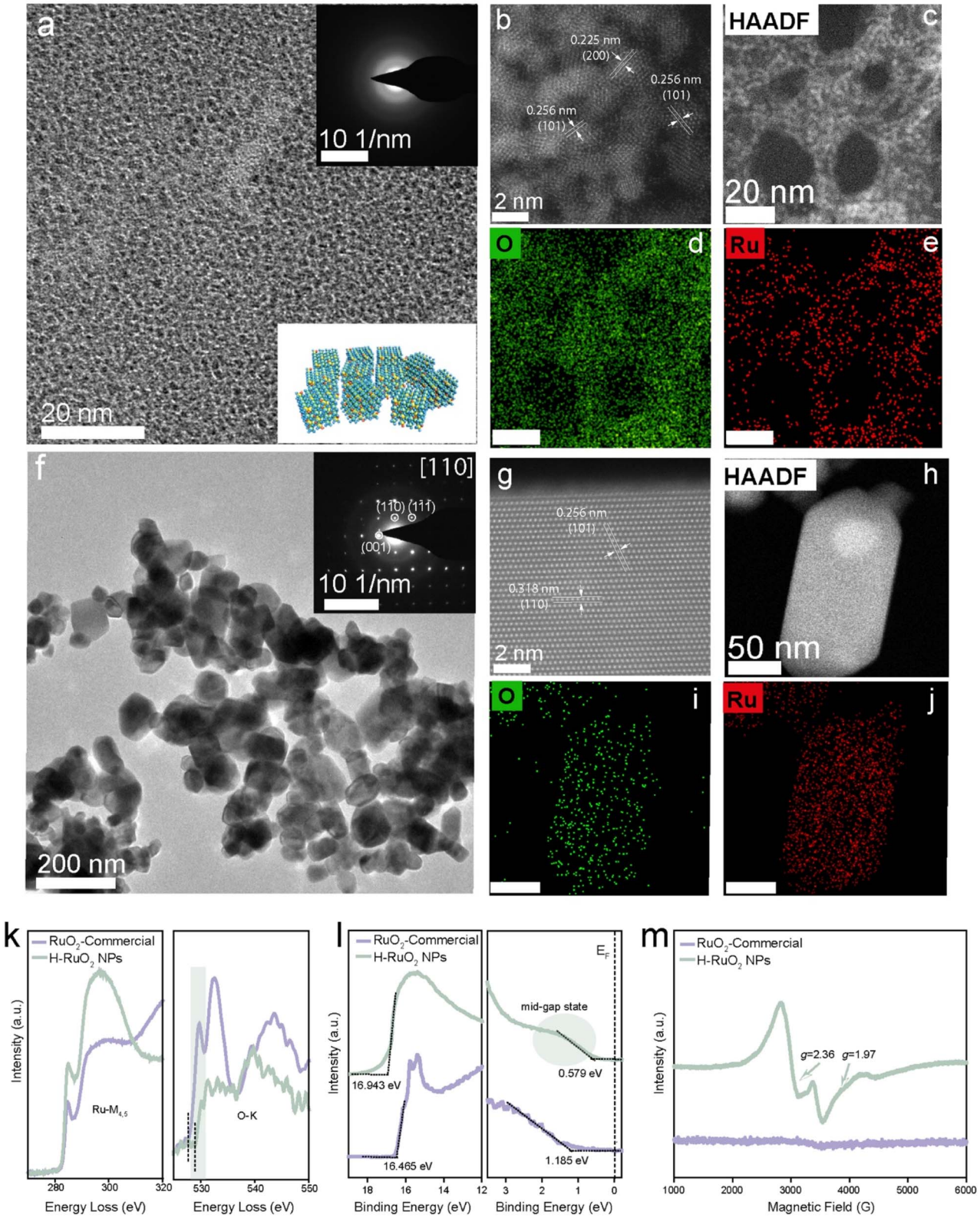

Fig. 2 Structural and compositional characterization of commercial and H–RuO_2 NPs. (a) TEM image of H–RuO_2 (inset shows the corresponding SAED pattern showing an amorphous nature). (b and c) HAADF-STEM images of H–RuO_2 at high (collected after a beam shower) and low magnifications. (d and e) EDX elemental mapping of H–RuO_2. (f) TEM image of commercial RuO_2 (inset displays the corresponding SAED pattern). (g and h) HAADF-STEM images of commercial RuO_2 at atomistic and low magnifications. (i and j) EDX elemental mapping of commercial RuO_2. (k) EELS spectra of the Ru-$M_{4,5}$ edge (left) and EELS spectra of the O-K edge (right) for commercial and H–RuO_2. (l) Photoemission cutoff (left) and valence band (right) UPS spectra of commercial and H–RuO_2. (m) EPR spectra of commercial and H–RuO_2.

could ionize and subsequently increase the density of carriers in the conduction band for subsequent redox reactions.[52] A relatively lower work function due to the removal of oxygen atoms in H–RuO_2 also indicates the nonstoichiometric nature of RuO_2. Electron paramagnetic resonance (EPR) spectroscopy was used to identify the oxygen vacancy-associated trapped electrons. As shown in Fig. 2m, a strong EPR signal at $g = 1.97$ was detected in H–RuO_2 NPs, which indicated the presence of unpaired electrons trapped in oxygen vacancies. The other paramagnetic centre at $g = 2.36$ was related to Ru^{3+} ions in the hydrous samples, thus corroborating the coexistence of both Ru^{3+} and oxygen vacancies. In contrast, no EPR signals were detected in commercial RuO_2.

The different metal nanostructures spontaneously produced on the surface of H–RuO_2 were analyzed *via* electron microscopy. The low-resolution and HRTEM images of H–RuO_2@Ag NPs are presented in Fig. 3a and b. Examination of the TEM and HAADF-STEM images unambiguously verified the spherical polycrystalline Ag NPs (20–30 nm) grown on H–RuO_2. Fig. 3c shows the compositional maps of Ag, Ru, and O. The product was also prepared under alkaline conditions (pH 9.0), and the morphology of the Ag NPs remained identical to that without changing the pH of the solution (Fig. S7†). Gold-based nanostructures obtained under varying pH conditions were examined; relatively large Au NPs were deposited onto the surface of H–RuO_2 in both acidic media, as shown in Fig. S8.† When the pH was increased to 9.0, unlike the structures produced under acidic conditions, the self-assembled structure of Au was convincingly evidenced in Fig. 3d and e. The self-assembled nanostructures were composed of numerous interconnected nanosized Au NPs (5–10 nm). The elemental distribution mapping of the Au nanostructure grown on H–RuO_2 is shown in Fig. 3f. The spontaneous reduction route was similarly employed to generate H–RuO_2@Pt nanostructures. Platinum ions were first selectively reduced on H–RuO_2 NPs and progressively grown to large spheres of Pt (50–100 nm) with self-assembled structures. The TEM images (Fig. 3g and h) reveal the interconnected Pt NPs and the elemental distribution mapping confirms the presence of Pt, Ru, and O.

Absorption spectroscopy was used to monitor the optical properties of RuO_2 materials before and after the deposition of metal nanostructures under different reaction conditions.

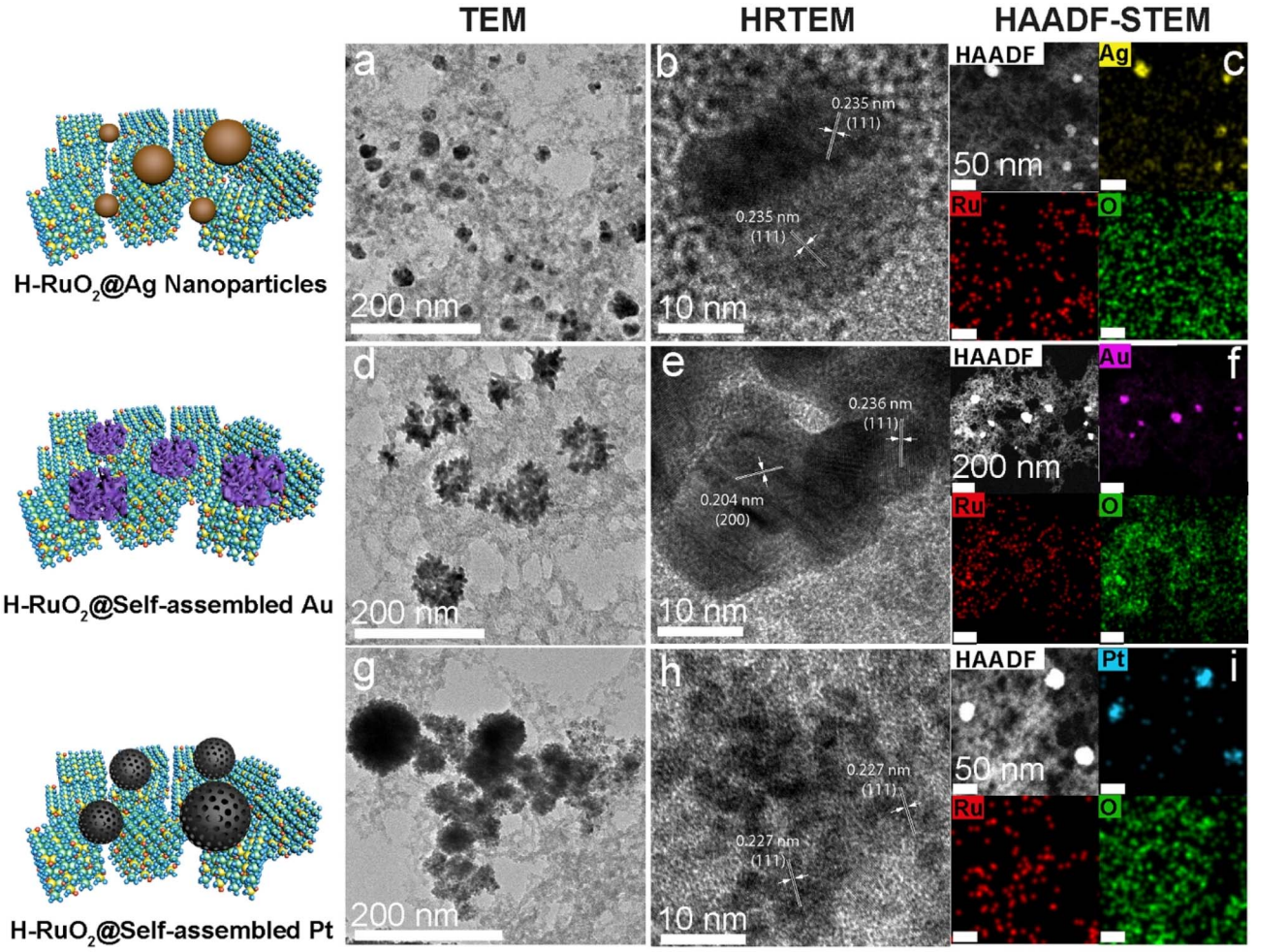

Fig. 3 Structural and compositional characterizations of spontaneously grown H–RuO_2@metal nanostructures by electron microscopy. (a and b) TEM and HRTEM images of H–RuO_2@Ag. (c) EDX elemental mapping of H–RuO_2@Ag. (d and e) TEM images of H–RuO_2@Au. (f) EDX elemental mapping of H–RuO_2@Au. (g and h) TEM images of H–RuO_2@Pt. (i) EDX elemental mapping of H–RuO_2@Pt.

Fig. 4a shows the characteristic absorption spectrum of H–RuO_2 NPs. After introducing the Ag^+ solution, the colour of the solution changed (inset of Fig. 4a), and the appearance of the absorption band at 419 nm associated with the surface plasmon resonance of Ag NPs indicated the formation of Ag NPs. The redox reaction between H–RuO_2 and an Au^{3+} salt in an acidic reaction medium produced a plasmon-associated absorption peak at 550 nm (Fig. S8†); when the pH was set to 5.0, no considerable fluctuation in the plasmonic band and colour of the solution was detected. However, a noticeable change in the intensity and position (620 nm) of the plasmonic peak was observed when the initial pH was increased to 9.0, verifying the generation of self-assembled Au under alkaline conditions (inset of Fig. 4a). The optical spectra of commercial RuO_2 before and after incubation with metal precursors under similar experimental conditions were also recorded. Fig. S9† shows the corresponding spectra and photos of the solutions; no metal-associated optical bands were observed, indicating the redox inactive nature of commercial RuO_2. The powder X-ray diffraction (PXRD) pattern (Fig. 4b) revealed a disordered (amorphous) nature of the H–RuO_2 NPs, whereas the appearance of sharp peaks implies the well-crystallized nature of commercial RuO_2 (JCPDS file no. 40-1290). Obvious diffraction peaks corresponding to the (111) and (200) planes of Ag were observed, while the peaks at 38.33° and 44.86° could be indexed to the face-centered cubic (fcc) structure of metallic Au (JCPDS file no. 04-0784). The XRD pattern of H–RuO_2@Pt displayed a distinct peak at 39.90° indexed to the (111) plane of Pt (JCPDS file no. 04-0802).

The oxidation state, chemical composition of the nanostructures, and the hydrous nature of the RuO_2 NPs were determined by X-ray photoelectron spectroscopy (XPS). The survey XPS spectra of commercial RuO_2 and the H–RuO_2-based nanostructures are provided in Fig. S10.† Because of the overlap of the XPS signals of Ru 3d photoelectrons with those of C 1s, the Ru 3p core-line spectrum was analysed instead for the examination. The XPS signals of Ru $3p_{3/2}$ and $3p_{1/2}$ were deconvoluted into four separate peaks: the two peaks at 462.7 and 484.8 eV were ascribed to Ru^{4+}, whereas the remaining two at 465.2 and 487.3 eV were related to Ru^{3+}, as shown in Fig. 4c.[53] The deconvoluted O 1s spectrum of H–RuO_2 exhibits three distinct components: the peak at 529.8 eV corresponds to lattice oxygen, whereas the two other peaks at 531.2 and 533 eV are linked to hydroxyl groups and confined water content, respectively (Fig. 4d). The XPS data revealed that H–RuO_2 contains an appreciable amount of trivalent hydrated species (Ru–O–H), whereas the commercial RuO_2 has a lower Ru^{3+} ratio (0.45) than hydrous NPs (1.13) but has a more pronounced lattice oxygen (Ru–O–Ru) component (Fig. S11†). As shown in Fig. S12a,† the doublet with distinct binding energies of 70.5 (Pt $4f_{7/2}$) and 73.9 eV (Pt $4f_{5/2}$) in H–RuO_2@Pt corresponded to metallic Pt^0. The growth of metallic Ag NPs was seen by observing the presence of representative peaks at 368.0 and 374.0 eV in the Ag 3d spectrum. The examination of H–RuO_2@Au showed two peaks at 84.0 and 88.0 eV, which could be attributed to Au $4f_{7/2}$ and Au $4f_{5/2}$, respectively (Fig. S12b and c†). After the redox reactions with metal precursors, we measured the changes in the composition of H–RuO_2 (Fig. S13†). A slight reduction in the

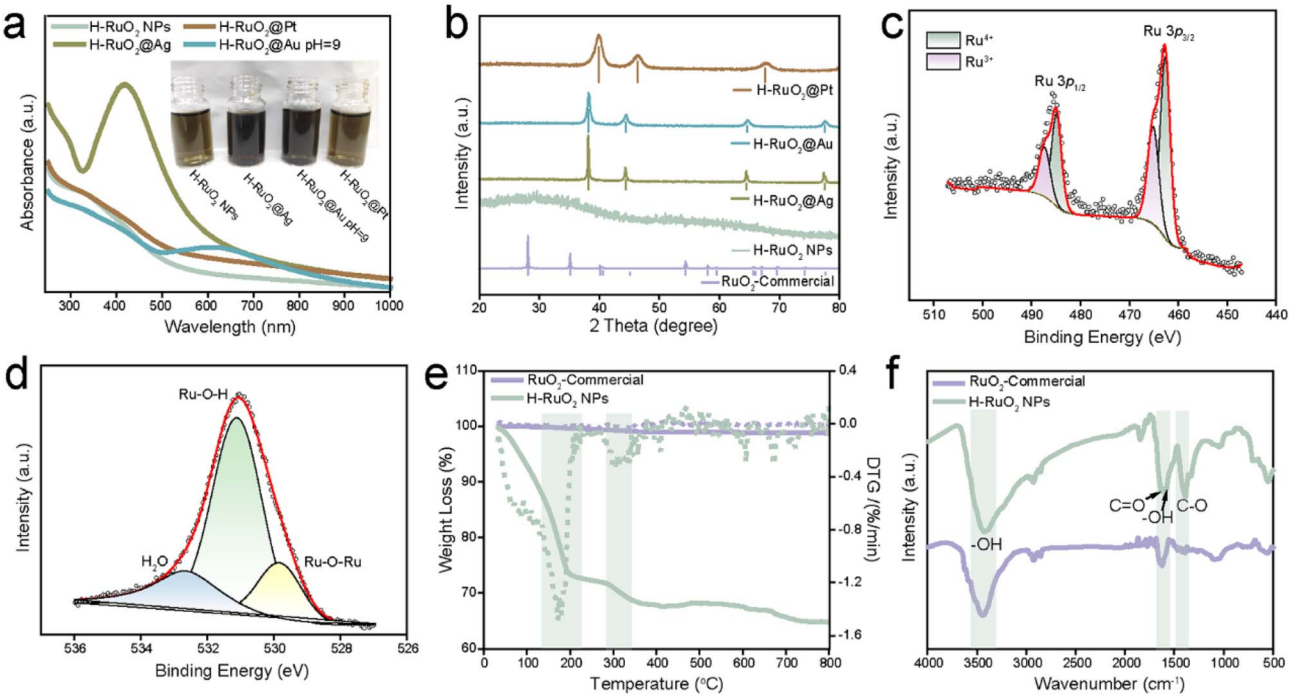

Fig. 4 Structural and compositional characterizations of spontaneously grown H–RuO_2@metal nanostructures. (a) UV-visible extinction spectra and the corresponding digital images (inset from left to right: H–RuO_2, H–RuO_2@Ag, H–RuO_2@Au, and H–RuO_2@Pt). (b) XRD patterns of commercial RuO_2, H–RuO_2, H–RuO_2@Ag, H–RuO_2@Au, and H–RuO_2@Pt. (c and d) High-resolution XPS spectra of H–RuO_2 Ru 3p and O 1s. (e) TGA-DTG thermal analysis of commercial and H–RuO_2. (f) FTIR spectra of citrate-modified commercial and H–RuO_2.

ratio of the Ru^{3+} component was observed in all three samples (from 1.13 to ~0.90).

Thermogravimetric analysis (TGA) was performed in the air to determine the water content in H–RuO_2 NPs (heating rate 10 °C min^{-1}). As shown in Fig. 4e, the weight loss occurred in stages; a more drastic weight loss (26.9%) was observed from 25 to 180 °C, followed by a gradual decay (4.3%) from 180 to 410 °C. The initial loss could readily be assigned to physical dehydration, while the second loss could be ascribed to chemical dehydration. These results suggested an overall composition of $RuO_2 \cdot 2.70H_2O$. In contrast, a nonsignificant weight loss from 25 to 800 °C in commercial RuO_2 was observed, demonstrating

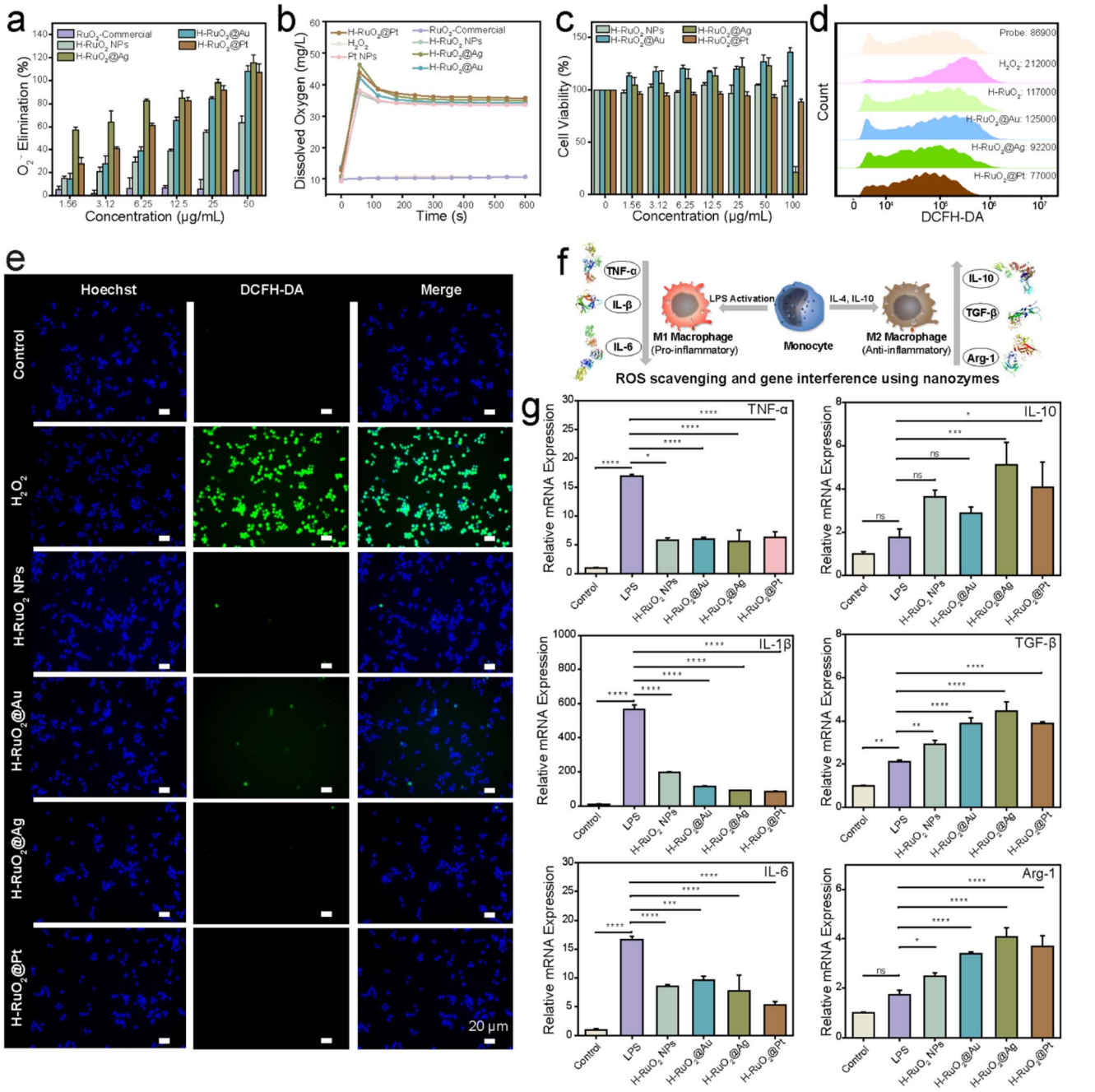

Fig. 5 Enzyme mimicking and ROS scavenging activities of H–RuO_2@metal nanozymes. (a and b) SOD- and CAT-like activities of different RuO_2-based nanozymes. (c) Cell viability of RAW 264.7 cells treated with different concentrations of H–RuO_2 and H–RuO_2@metal nanozymes. (d) Flow cytometry for the evaluation of ROS scavenging in RAW 264.7 cells upon treatment with H–RuO_2 and H–RuO_2@metal nanozymes (25 μg mL^{-1}). (e) Fluorescence images demonstrating ROS scavenging after nanozyme treatments (DCFH-DA and Hoechst were used as the ROS probe and nucleus dye respectively). (f) Schematic representation exemplifying the M1 and M2 polarization of macrophages, and gene interference following nanozyme treatment. (g) Anti-inflammatory effect of H–RuO_2 and H–RuO_2@metal nanozymes (10 μg mL^{-1}) on the mRNA levels of pro-inflammatory (TNF-α, IL-1β, and IL-6) and anti-inflammatory (IL-10, TGF-β, and Arg-1) cytokines. Data are shown as means ± SD (n = 3). Statistical analysis was performed using one-way ANOVA, and specific P-values are shown in the source data.

the absence of confined water as well as the crystalline nature of the sample, as seen in the XRD results. The FT-IR absorption spectra of both RuO_2 samples showed the surface-bound carboxylate and hydroxide species in H–RuO_2. As displayed in Fig. 4f, the bands (1384 and 1623 cm^{-1}) associated with the carboxylic group of citrate could be seen. The absorption bands at ~1604 and 3384 cm^{-1} were assigned to the surface hydroxyl group and confined molecular water present in H–RuO_2. The chemical structures of both RuO_2 samples were also analyzed *via* Raman spectroscopy. Three well-defined Raman peaks located at 521, 629, and 690 cm^{-1}, assigned to the E_g, A_{1g}, and B_{2g} modes, respectively, were detected in the commercial sample. On the other hand, broader and weaker Raman-active modes were observed in H–RuO_2, suggesting the local lattice defectiveness and short-range order (Fig. S14†).[46] Zeta potential measurements showed negative potentials (−31.3 mV in H–RuO_2 and −5.3 mV in the commercial RuO_2 sample) in both samples implying the chemisorption of multidentate citrate groups (Fig. S15†). The atomic ratio between Ru and the three metals was determined by inductively coupled plasma atomic emission spectroscopy (ICP-AES), and the amounts of Ag, Au, and Pt were found to be 85.0, 150.7, and 207.6 mg per g of H–RuO_2 NPs, respectively.

The multi-nanozymatic activities of the RuO_2-based nanostructures were evaluated; H–RuO_2@metal displayed appreciable POD-like activities, and the relative activities determined at different pH values are shown in Fig. S16.† The kinetics of H–RuO_2@metal nanostructures were also compared to those of well-known POD-like nanozymes (Fe_3O_4 and Pt NPs). We measured the SOD *via* the WST-1 kit; in principle the xanthine oxidase (XO) catalyzes the reaction between water-soluble tetrazolium WST-1 and $O_2^{\bullet-}$ to generate a formazan dye. The presence of an SOD-like nanozyme inhibits this reaction. Fig. 5a shows the scavenging ability of H–RuO_2@metal nanozymes against $O_2^{\bullet-}$. Of the samples, H–RuO_2@Pt and H–RuO_2@Ag displayed superior SOD-like activities. As low as 1.56 μg mL^{-1} of H–RuO_2@Ag scavenged ~60% of the $O_2^{\bullet-}$ species. The CAT-like activities of the nanostructures were monitored by quantifying the decomposition of H_2O_2 using a dissolved oxygen meter. As shown in Fig. 5b, the H–RuO_2 NPs exhibited excellent CAT-like activity, as high as displayed by a classic CAT-like nanozyme (Pt NPs). The reaction kinetics data were acquired to validate the excellent CAT-like enzymatic behavior of H–RuO_2@metal nanostructures (Fig. S17†). Since the H–RuO_2 support showed exceptional activity, the CAT-like activities of all the resulting RuO_2-based nanozymes were understandably comparable to that of H–RuO_2. The CAT-like activities were also evaluated at different pH values, and the findings show that by lowering the pH value, the CAT-like activity correspondingly decreases (Fig. S18†). Notably, the naked surfaces of metal nanostructures and their intimate contact with the H–RuO_2 support most likely resulted in the enhancement of biocatalytic activities. In contrast to the enzymatic activities of H–RuO_2 samples, the SOD- and CAT-like activities of commercial RuO_2 were negligible (Fig. 5b). The excellent multienzyme-like activities of H–RuO_2@metal nanostructures provided us with the impetus to explore them for cytoprotective and anti-inflammatory effects. The cytotoxicity of H–RuO_2@metal nanozymes was first tested against RAW264.7 cells using a CCK-8 assay (Fig. 5c), and the nanozymes exhibited low cellular toxicity.

The ROS-scavenging ability against oxidative stress induced by H_2O_2 was then assessed. A strong intracellular fluorescence was observed in cells treated with H_2O_2 using the ROS probe 2′,7′-dichlorodihydrofluorescein diacetate (DCFH-DA). Following the incubation with the H–RuO_2@metal nanozymes (25 μg mL^{-1}), we observed a significant decline in fluorescence intensity (Fig. 5d). The treated cells were also examined under a fluorescence microscope, and a noticeable quenching of green fluorescence was observed particularly in H–RuO_2@Pt and H–RuO_2@Ag samples (Fig. 5e). The *in vitro* anti-inflammatory activities of H–RuO_2@metal nanozymes were evaluated *via* qPCR analysis. Under bacterial threat or other stimulations such as ROS, the dormant form of macrophages is switched to either the M1 state to release inflammatory cytokines such as IL-1β, IL-6, and TNF-α or the M2 phenotype to promote tissue repair and wound healing by releasing anti-inflammatory molecular messengers such as IL-10, TGF-β, and Arg-1 (Fig. 5f). As shown in Fig. 5g, after LPS stimulation, the mRNA expression of three typical pro-inflammatory factors (TNF-α, IL-1β, and IL-6) was upregulated by 17-, 567-, and 16-fold, respectively. Subsequent treatment with H–RuO_2@metal nanozymes resulted in a marked reduction in those M1 markers. At the same time, a noticeable upregulation in anti-inflammatory M2 markers (*i.e.*, IL-10, TGF-β, and Arg-1) was also observed, especially after treatment with H–RuO_2@Ag and H–RuO_2@Pt ($P < 0.001$) (Table S2†).

As a proof of concept, we utilized the encouraging *in vitro* anti-inflammatory activities for relieving two representative forms of (IBD)—Crohn's disease (CD) and ulcerative colitis (UC). To induce CD, sensitization and enema with 2,4,6-trinitrobenzene sulfonic acid sol (TNBS) were administered, as illustrated in Fig. 6a. On day 9 after the establishment of the CD model, various nanozymes were orally administered for three consecutive days. The therapeutic efficacy of the nanozymes was investigated by evaluating the changes in body weight, colon length, and levels of pro-inflammatory cytokines and analyzing the histologically stained colon sections. Significant weight loss and the shortening of the colon length (from 55.21 ± 2.76 to 42.60 ± 5.58 mm) were observed on day 8, indicating the successful establishment of CD. Later, three days of treatment with H–RuO_2@metal nanozymes led to a noticeable recovery in body weight (Fig. 6b). An apparent recovery in colon lengths to normal levels was also observed (especially in the case of H–RuO_2@Ag and H–RuO_2@Pt, $P < 0.0001$), as shown in Fig. 6c and f. The levels of both IL-1β and TNF-α were increased in CD-induced mice; in contrast, a significant downregulation was detected in RuO_2@metal-treated groups, as shown in Fig. 6d and e. The H–RuO_2@Ag and H–RuO_2@Pt nanozymes exerted the maximum anti-inflammatory activities ($P < 0.0001$). In the representative slices of the colon of each experimental group, the histological appearance of the control and sham groups remained intact with no detachment or loss of intestinal mucosa, whereas severe intestinal tissue damage in CD-induced mice was noticed. An obvious improvement in the histological

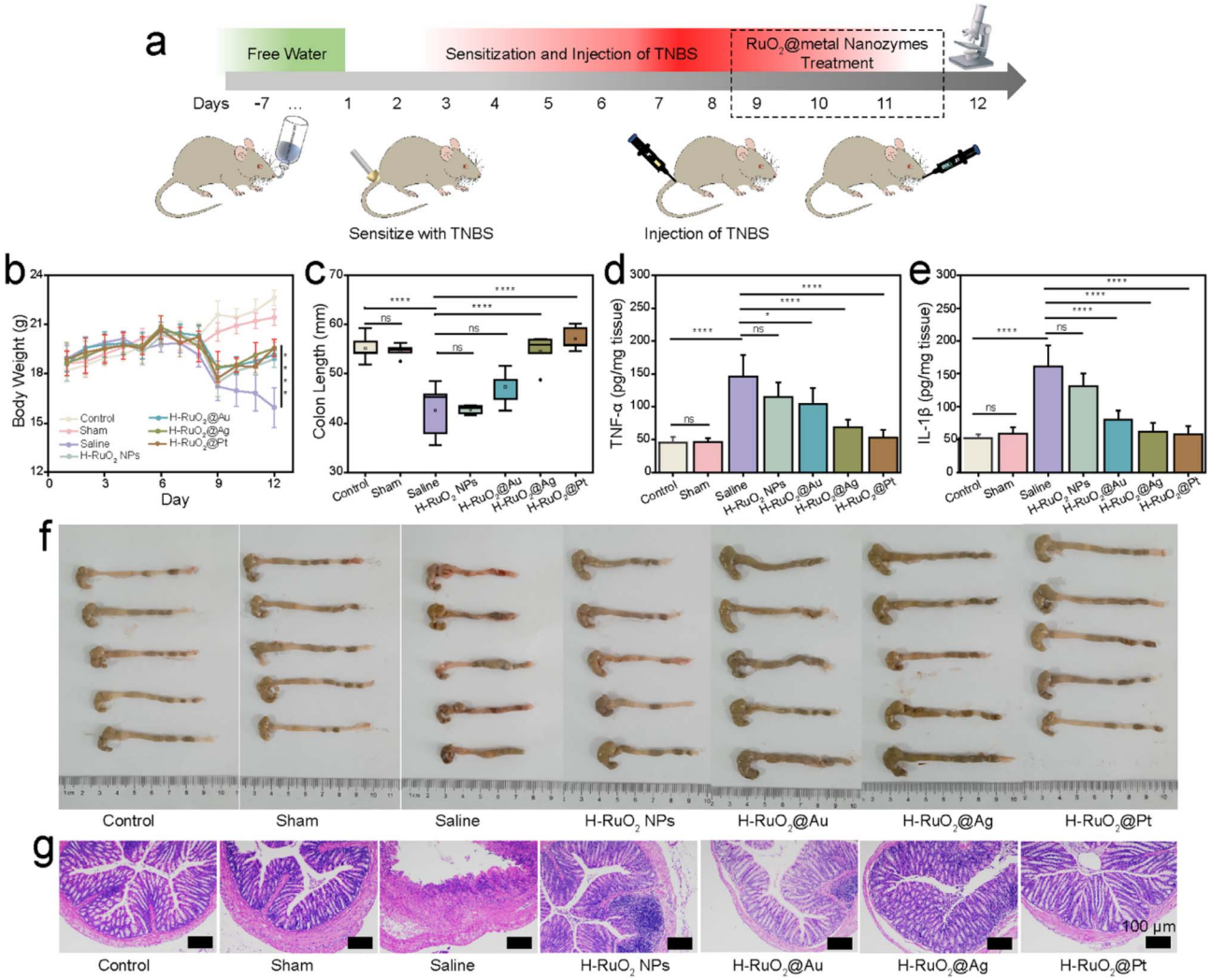

Fig. 6 Evaluation of anti-inflammatory therapy in Crohn's disease model. (a) Overall protocol for induction and treatment of CD. (b) Daily body weight recorded while undergoing treatments with different H–RuO_2@metal nanozymes. (c) Statistical length of the colon taken on day 12. (d and e) Local concentrations of proinflammatory cytokines IL-1β and TNF-α in colon homogenates. (f) Representative images of colons taken on day 12. (g) H&E-stained sections of colons following H–RuO_2@metal nanozymes treatment. Data are shown as means ± SD ($n = 5$). Statistical analysis was performed using one-way ANOVA; specific P-values are shown in the source data.

appearance can be seen in hematoxylin and eosin (H&E)-stained colon sections of nanozyme-treated groups (Fig. 6g).

In another IBD model, dextran sulphate sodium (DSS) was used to induce UC. The body weight was remarkably decreased along with the shortening of colon lengths (from 61.79 ± 4.1 to 47.63 ± 3.4 mm) after six days of DSS administration. After the treatment with H–RuO_2@metal nanozymes, a noticeable improvement in the body weights of UC-induced mice was observed (Fig. 7b). Moreover, restoration of the colon length to normal limits ($P < 0.0001$) was also observed, as shown in Fig. 7c and f. A statistically significant downregulation in IL-1β and TNF-α concentrations was detected in H–RuO_2@Ag- and H–RuO_2@Pt-treated groups ($P < 0.05$) (Fig. 7d and e). H&E-stained colon tissue sections from the H–RuO_2@metal-treated groups demonstrated alleviation of tissue destruction and inflammation (Fig. 7g). To evaluate the biosafety, the *in vivo* toxicity of RuO_2-based nanozymes was studied through histopathological observations. H&E-stained sections of the heart, liver, spleen, lungs, and kidney showed no apparent difference from the control group in either UC or CD models (Fig. S19 and S20†). To assess the biodistribution and biodegradation of H–RuO_2@metal nanostructures, H–RuO_2 and H–RuO_2@Ag were orally administered. Following different periods (12, 24, 48, and 72 h), the mice were sacrificed, and their blood, faeces, and tissues of the heart, liver, spleen, lungs, kidney, and colon were dissolved in acid. However, due to the inability of ruthenium to make a stable compound with nitric acid (ruthenium nitrate), we indirectly determined the biodistribution and biodegradation in terms of Ag content using ICP-OES (Fig. S21†). The highest concentration of Ag was detected in faeces, indicating that most of the nanozymes were excreted from the body *via* faeces.

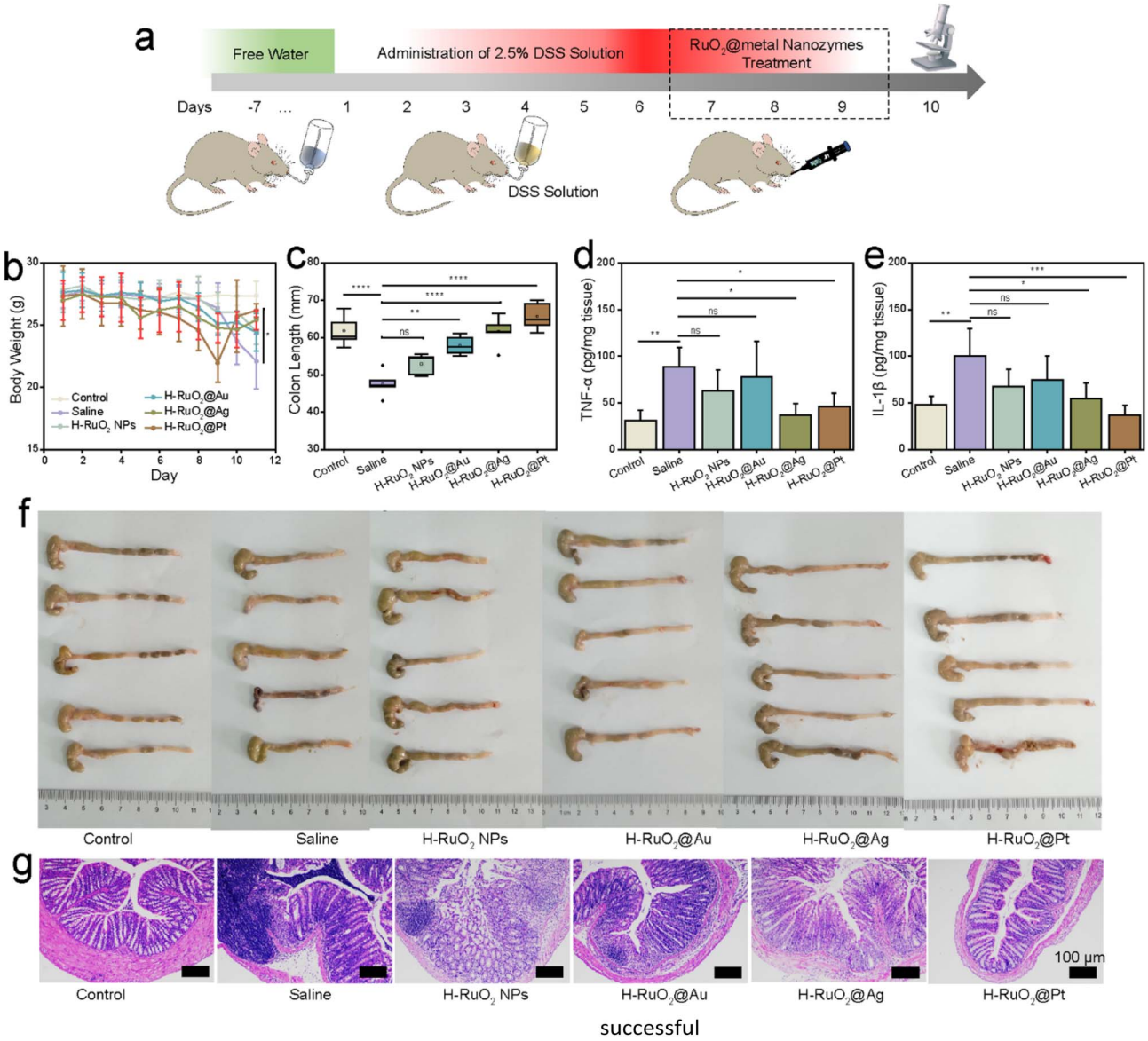

Fig. 7 Evaluation of anti-inflammatory therapy in the ulcerative colitis disease model. (a) Overall protocol for induction and treatment of UC. (b) Daily body weight recorded while undergoing treatments with different H–RuO_2@metal nanozymes. (c) Statistical length of the colon taken on day 10. (d and e) Local concentrations of proinflammatory cytokines IL-1β and TNF-α in colon homogenates. (f) Representative images of the colon taken on day 10. (g) H&E-stained sections of colons following H–RuO_2@metal nanozyme treatment. Data are shown as means ± SD (n = 5). Statistical analysis was performed using one-way ANOVA, and specific P-values are shown in the source data.

Conclusions

In summary, we presented the ultrasmall RuO_2 as a reactive oxide to spontaneously grow multiple metallic nanostructures. Unlike previous studies, RuO_2 NPs not only generated noble metals at room temperature but also produced Au and Pt with self-assembled structures by merely tuning the synthetic conditions. The experimental findings indicated that the presence of oxygen vacancies and the amorphous nature of the H–RuO_2 NPs prompted the heterogeneous interfacial redox reactions between reactive oxide and oxidative metal precursors. The excellent biocatalytic features of H–RuO_2@metal were then used for treating IBDs. Both H–RuO_2@Ag and H–RuO_2@Pt nanozymes displayed appreciable therapeutic performance at a dose of 1.0 mg kg^{-1} in both UC and CD models. The development of a convenient strategy to produce oxide-supported metal nanostructures is indeed a significant technological requirement, and our developed approach can be a step forward in this direction.

Data availability

Data supporting this study is available in the ESI† and further details are available from the authors on reasonable request.

Author contributions

F. M. conceived the idea and synthesized and characterized the materials. H. W. supervised the work. X. C. carried out *in vitro*

and *in vivo* experiments. J. T. performed the electron microscopic studies. Y. C. carried out *in vivo* investigations. Y. L. performed the *in vitro* experiment. C. Z. assisted in the characterization. Y. Z. assisted with and commented on the manuscript. L. M. assisted in *in vitro* experiments. Y. D. assisted in the microscopic characterization. F. M. wrote the first draft of the manuscript and H. W. provided the major revisions. All the authors discussed the results and commented on the manuscript.

Conflicts of interest

The authors declare no competing interests.

Acknowledgements

This work was supported by the Jiangsu Provincial Key R&D Program-Social Development (BE2022836), National Key R&D Program of China (2019YFA0709200 and 2021YFF1200700), National Natural Science Foundation of China (22374071 and 11874199), PAPD Program, State Key Laboratory of Analytical Chemistry for Life Science (5431ZZXM2306), and Fundamental Research Funds for the Central Universities (202200325 and 021314380228). The writing was polished with the assistance of OpenAI. All animal studies were approved by the Institutional Animal Care and Use Committee (IACUC) of Nanjing University.

Notes and references

1 X. Wang, S. Song and H. Zhang, A redox interaction-engaged strategy for multicomponent nanomaterials, *Chem. Soc. Rev.*, 2020, **49**, 736–764.
2 M. R. Buck and R. E. Schaak, Emerging strategies for the total synthesis of inorganic nanostructures, *Angew. Chem., Int. Ed.*, 2013, **52**, 6154–6178.
3 S. Rawalekar and T. Mokari, Rational design of hybrid nanostructures for advanced photocatalysis, *Adv. Energy Mater.*, 2013, **3**, 12–27.
4 M. R. Buck, J. F. Bondi and R. E. Schaak, A total-synthesis framework for the construction of high-order colloidal hybrid nanoparticles, *Nat. Chem.*, 2012, **4**, 37–44.
5 A. L. M. Reddy, S. R. Gowda, M. M. Shaijumon and P. M. Ajayan, Hybrid nanostructures for energy storage applications, *Adv. Mater.*, 2012, **24**, 5045–5064.
6 T. Mokari, E. Rothenberg, I. Popov, R. Costi and U. Banin, Selective growth of metal tips onto semiconductor quantum rods and tetrapods, *Science*, 2004, **304**, 1787–1790.
7 X. Li, L. Chen, D. Cui, W. Jiang, L. Han and N. Niu, Preparation and application of Janus nanoparticles: recent development and prospects, *Coord. Chem. Rev.*, 2022, **454**, 214318.
8 C. C. Crane, R. H. Manso, J. Li, M. Benamara, J. Tao, Y. Zhu, F. Wang and J. Chen, A metal-on-metal growth approach to metal–metal oxide core–shell nanostructures with plasmonic properties, *J. Phys. Chem. C*, 2020, **124**, 17191–17203.
9 F. Shaik, Ligand-free yolk-shell nanoparticles: synthesis and catalytic applications, *ChemNanoMat*, 2020, **6**, 1449–1473.
10 T. A. Gschneidtner, S. Lerch, E. Olsén, X. Wen, A. C. Y. Liu, A. Stolaś, J. Etheridge, E. Olsson and K. Moth-Poulsen, Constructing a library of metal and metal–oxide nanoparticle heterodimers through colloidal assembly, *Nanoscale*, 2020, **12**, 11297–11305.
11 D. Jishkariani, Y. Wu, D. Wang, Y. Liu, A. van Blaaderen and C. B. Murray, Preparation and self-assembly of dendronized janus Fe_3O_4–Pt and Fe_3O_4–Au heterodimers, *ACS Nano*, 2017, **11**, 7958–7966.
12 M. N. Tahir, F. Natalio, M. A. Cambaz, M. Panthöfer, R. Branscheid, U. Kolb and W. Tremel, Controlled synthesis of linear and branched Au@ZnO hybrid nanocrystals and their photocatalytic properties, *Nanoscale*, 2013, **5**, 9944–9949.
13 X. Pan, Z. Fan, W. Chen, Y. Ding, H. Luo and X. Bao, Enhanced ethanol production inside carbon-nanotube reactors containing catalytic particles, *Nat. Chem.*, 2007, **6**, 507–511.
14 B. Puértolas, M. Comesaña-Hermo, L. V. Besteiro, M. Vázquez-González and M. A. Correa-Duarte, Challenges and opportunities for renewable ammonia production *via* plasmon-assisted photocatalysis, *Adv. Energy Mater.*, 2022, **12**, 2103909.
15 A. Gellé, T. Jin, L. de la Garza, G. D. Price, L. V. Besteiro and A. Moores, Applications of plasmon-enhanced nanocatalysis to organic transformations, *Chem. Rev.*, 2020, **120**, 986–1041.
16 X. Liu, J. Iocozzia, Y. Wang, X. Cui, Y. Chen, S. Zhao, Z. Li and Z. Lin, Noble metal–metal oxide nanohybrids with tailored nanostructures for efficient solar energy conversion, photocatalysis and environmental remediation, *Energy Environ. Sci.*, 2017, **10**, 402–434.
17 Z.-c. Zhang, B. Xu and X. Wang, Engineering nanointerfaces for nanocatalysis, *Chem. Soc. Rev.*, 2014, **43**, 7870–7886.
18 M. Cargnello, V. V. T. Doan-Nguyen, T. R. Gordon, R. E. Diaz, E. A. Stach, R. J. Gorte, P. Fornasiero and C. B. Murray, Control of metal nanocrystal size reveals metal-support interface role for ceria catalysts, *Science*, 2013, **341**, 771–773.
19 M. Cueto, M. Sanz, M. Oujja, F. Gámez, B. Martínez−Haya and M. Castillejo, Platinum nanoparticles prepared by laser ablation in aqueous solutions: fabrication and application to laser desorption ionization, *J. Phys. Chem. C*, 2011, **115**, 22217–22224.
20 J. Singh, K. Sahu, A. Pandey, M. Kumar, T. Ghosh, B. Satpati, T. Som, S. Varma, D. K. Avasthi and S. Mohapatra, Atom beam sputtered Ag-TiO_2 plasmonic nanocomposite thin films for photocatalytic applications, *Appl. Surf. Sci.*, 2017, **411**, 347–354.
21 M. Hao, Y. Wang, D. Chen, D. Wu, P. Li and H. Zhang, Ion implantation synthesis of long-term stable high-entropy metallic glass nanoparticles, *J. Alloys Compd.*, 2022, **906**, 164303.
22 Y. Yao, Z. Huang, P. Xie, S. D. Lacey, R. J. Jacob, H. Xie, F. Chen, A. Nie, T. Pu, M. Rehwoldt, D. Yu, M. R. Zachariah, C. Wang, R. Shahbazian-Yassar, J. Li and

L. Hu, Carbothermal shock synthesis of high-entropy-alloy nanoparticles, *Science*, 2018, **359**, 1489–1494.

23 Y. Shiraishi, H. Sakamoto, Y. Sugano, S. Ichikawa and T. Hirai, Pt–Cu bimetallic alloy nanoparticles supported on anatase TiO_2: highly active catalysts for aerobic oxidation driven by visible light, *ACS Nano*, 2013, **7**, 9287–9297.

24 N. Dimitratos, J. A. Lopez-Sanchez and G. J. Hutchings, Selective liquid phase oxidation with supported metal nanoparticles, *Chem. Sci.*, 2012, **3**, 20–44.

25 T. Barakat, J. C. Rooke, H. L. Tidahy, M. Hosseini, R. Cousin, J.-F. Lamonier, J.-M. Giraudon, G. De Weireld, B.-L. Su and S. Siffert, Noble-metal-based catalysts supported on zeolites and macro-mesoporous metal oxide supports for the total oxidation of volatile organic compounds, *ChemSusChem*, 2011, **4**, 1420–1430.

26 S. M. Kim, M. Jeon, K. W. Kim, J. Park and I. S. Lee, Postsynthetic functionalization of a hollow silica nanoreactor with manganese oxide-immobilized metal nanocrystals inside the cavity, *J. Am. Chem. Soc.*, 2013, **135**, 15714–15717.

27 F. Muhammad, F. Huang, Y. Cheng, X. Chen, Q. Wang, C. Zhu, Y. Zhang, X. Yang, P. Wang and H. Wei, Nanoceria as an electron reservoir: spontaneous deposition of metal nanoparticles on oxides and their anti-inflammatory activities, *ACS Nano*, 2022, **16**, 20567–20576.

28 Y. Zhu, X. Zhang, K. Koh, L. Kovarik, J. L. Fulton, K. M. Rosso and O. Y. Gutiérrez, Inverse iron oxide/metal catalysts from galvanic replacement, *Nat. Commun.*, 2020, **11**, 3269.

29 X. Pan and Y.-J. Xu, Efficient thermal- and photocatalyst of Pd nanoparticles on TiO_2 achieved by an oxygen vacancies promoted synthesis strategy, *ACS Appl. Mater. Interfaces*, 2014, **6**, 1879–1886.

30 M. H. Oh, T. Yu, S.-H. Yu, B. Lim, K.-T. Ko, M.-G. Willinger, D.-H. Seo, B. H. Kim, M. G. Cho, J.-H. Park, K. Kang, Y.-E. Sung, N. Pinna and T. Hyeon, Galvanic replacement reactions in metal oxide nanocrystals, *Science*, 2013, **340**, 964–968.

31 G. Xi, J. Ye, Q. Ma, N. Su, H. Bai and C. Wang, *In situ* growth of metal particles on 3D urchin-like WO_3 nanostructures, *J. Am. Chem. Soc.*, 2012, **134**, 6508–6511.

32 M. Zandieh and J. Liu, Nanozyme catalytic turnover and self-limited reactions, *ACS Nano*, 2021, **15**, 15645–15655.

33 Y. Liu, Y. Cheng, H. Zhang, M. Zhou, Y. Yu, S. Lin, B. Jiang, X. Zhao, L. Miao, C.-W. Wei, Q. Liu, Y.-W. Lin, Y. Du, C. J. Butch and H. Wei, Integrated cascade nanozyme catalyzes *in vivo* ROS scavenging for anti-inflammatory therapy, *Sci. Adv.*, 2020, **6**, eabb2695.

34 X. Zhang, Y. Liu, S. Gopalakrishnan, L. Castellanos-Garcia, G. Li, M. Malassiné, I. Uddin, R. Huang, D. C. Luther, R. W. Vachet and V. M. Rotello, Intracellular activation of bioorthogonal nanozymes through endosomal proteolysis of the protein corona, *ACS Nano*, 2020, **14**, 4767–4773.

35 H. Wei and E. Wang, Nanomaterials with enzyme-like characteristics (nanozymes): next-generation artificial enzymes, *Chem. Soc. Rev.*, 2013, **42**, 6060–6093.

36 L. Gao, J. Zhuang, L. Nie, J. Zhang, Y. Zhang, N. Gu, T. Wang, J. Feng, D. Yang, S. Perrett and X. Yan, Intrinsic peroxidase-like activity of ferromagnetic nanoparticles, *Nat. Nanotechnol.*, 2007, **2**, 577–583.

37 W. Chen, S. Li, J. Wang, K. Sun and Y. Si, Metal and metal-oxide nanozymes: bioenzymatic characteristics, catalytic mechanism, and eco-environmental applications, *Nanoscale*, 2019, **11**, 15783–15793.

38 J. Zhu, X. Peng, W. Nie, Y. Wang, J. Gao, W. Wen, J. N. Selvaraj, X. Zhang and S. Wang, Hollow copper sulfide nanocubes as multifunctional nanozymes for colorimetric detection of dopamine and electrochemical detection of glucose, *Biosens. Bioelectron.*, 2019, **141**, 111450.

39 J. Wu, Y. Yu, Y. Cheng, C. Cheng, Y. Zhang, B. Jiang, X. Zhao, L. Miao and H. Wei, Ligand-dependent activity engineering of glutathione peroxidase-mimicking MIL-47(V) metal–organic framework nanozyme for therapy, *Angew. Chem., Int. Ed.*, 2021, **60**, 1227–1234.

40 J. Mu, L. He, W. Fan, W. Tang, Z. Wang, C. Jiang, D. Zhang, Y. Liu, H. Deng, J. Zou, O. Jacobson, J. Qu, P. Huang and X. Chen, Cascade reactions catalyzed by planar metal–organic framework hybrid architecture for combined cancer therapy, *Small*, 2020, **16**, 2004016.

41 L. Huang, J. Chen, L. Gan, J. Wang and S. Dong, Single-atom nanozymes, *Sci. Adv.*, 2019, **5**, eaav5490.

42 H. Sun, Y. Zhou, J. Ren and X. Qu, Carbon nanozymes: enzymatic properties, catalytic mechanism, and applications, *Angew. Chem., Int. Ed.*, 2018, **57**, 9224–9237.

43 C. Wu, X. Han, W. Feng, Z. Liu, L. Chen, B. Zhou, Y. Chen and J. Shi, Multi-enzymatic activities of ultrasmall ruthenium oxide for anti-inflammation and neuroprotection, *Chem. Eng. J.*, 2021, **411**, 128543.

44 S. Laha, Y. Lee, F. Podjaski, D. Weber, V. Duppel, L. M. Schoop, F. Pielnhofer, C. Scheurer, K. Müller, U. Starke, K. Reuter and B. V. Lotsch, Ruthenium oxide nanosheets for enhanced oxygen evolution catalysis in acidic medium, *Adv. Energy Mater.*, 2019, **9**, 1803795.

45 Y. Lin, Z. Tian, L. Zhang, J. Ma, Z. Jiang, B. J. Deibert, R. Ge and L. Chen, Chromium-ruthenium oxide solid solution electrocatalyst for highly efficient oxygen evolution reaction in acidic media, *Nat. Commun.*, 2019, **10**, 162.

46 Y. Wang, H. Li, W. Zhou, X. Zhang, B. Zhang and Y. Yu, Structurally disordered RuO_2 nanosheets with rich oxygen vacancies for enhanced nitrate electroreduction to ammonia, *Angew. Chem., Int. Ed.*, 2022, **61**, e202202604.

47 L. Zhang, H. Jang, H. Liu, M. G. Kim, D. Yang, S. Liu, X. Liu and J. Cho, Sodium-decorated amorphous/crystalline RuO_2 with rich oxygen vacancies: a robust pH-universal oxygen evolution electrocatalyst, *Angew. Chem., Int. Ed.*, 2021, **60**, 18821–18829.

48 W. Dmowski, T. Egami, K. E. Swider-Lyons, C. T. Love and D. R. Rolison, Local atomic structure and conduction mechanism of nanocrystalline hydrous RuO_2 from X-ray scattering, *J. Phys. Chem. B*, 2002, **106**, 12677–12683.

49 G. Wang, Y. Yang, D. Han and Y. Li, Oxygen defective metal oxides for energy conversion and storage, *Nano Today*, 2017, **13**, 23–39.

50 F. Zuo, L. Wang, T. Wu, Z. Zhang, D. Borchardt and P. Feng, Self-doped Ti^{3+} enhanced photocatalyst for hydrogen

production under visible light, *J. Am. Chem. Soc.*, 2010, **132**, 11856–11857.

51 Y. Wan, Y. Li, K. Wang, H. Liu, H. Hu and M. Wu, Oxygen-deficient metal oxides for supercapacitive energy storage: from theoretical calculation to structural regulation and utilization, *Adv. Energy Sustainable Res.*, 2022, **3**, 2100221.

52 Y. Hou, X. Du, S. Scheiner, D. P. McMeekin, Z. Wang, N. Li, M. S. Killian, H. Chen, M. Richter, I. Levchuk, N. Schrenker, E. Spiecker, T. Stubhan, N. A. Luechinger, A. Hirsch, P. Schmuki, H.-P. Steinrück, R. H. Fink, M. Halik, H. J. Snaith and C. J. Brabec, A generic interface to reduce the efficiency-stability-cost gap of perovskite solar cells, *Science*, 2017, **358**, 1192–1197.

53 W. Wang, S. Guo, I. Lee, K. Ahmed, J. Zhong, Z. Favors, F. Zaera, M. Ozkan and C. S. Ozkan, Hydrous ruthenium oxide nanoparticles anchored to graphene and carbon nanotube hybrid foam for supercapacitors, *Sci. Rep.*, 2014, **4**, 4452.